PS/AA/ACOL Note 84-14
HR/mp

15th September 1984

Pinch dynamics in a plasma lens: Description with a modified snowplow model and comparison with experimental results

E. Boggasch*, G. Miano**, H. Riege*

* CERN
** University of Naples

Abstract

A modified snowplow model is applied to the pinch dynamics in a plasma lens. Combined with the electrical circuit equations the model is adapted to and dealt with by the IBM SCEPTRE computer program, where pinch radius, current sheet velocity and current sheet acceleration are handled as state variables like currents and voltages. The computations are compared with experimental results obtained with a test pulse generator, where plasma lens current and voltage waveforms, as well as magnetic field distributions have been measured.

The agreements and the discrepancies between computations and measurements are discussed. The usefulness of the model for extrapolating to future plasma lens configurations is proven and improvements are recommended.

1. Introduction

The motivation to develop plasma lenses for the ACOL target area has been pointed out in the references 1), 2) and 3). Plasma lenses are superior to metal lenses provided they can be built such to stay alive for a sufficiently long time. The purpose of this note is to show that the pinch dynamics and stability problems of the current conducting plasma column can be mastered. Amongst several simple theoretical models describing the contraction process in a z-pinch we selected one which shows the best qualitative and quantitative agreement with our experimental results. Two prototype plasma lenses have been studied so far:

i) a 200 mm long lens with 40 mm inner diameter and
ii) a 250 mm long lens with 236 mm inner diameter.

The volume of prototype II is 44 times larger than that of prototype I and the ratio of the minimum observed contraction radii of both plasma columns is of the same order. Waveforms of current and voltage have been measured across both lenses. Streakphotos have only been taken on prototype I, whereas magnetic field distributions $B_\phi(r,t)$ have only been measured on prototype II. Pinch radii can be extracted from all three types of measurements. When a theoretical model allows to predict the observed dynamics in both prototypes to some degree, we are capable to extrapolate from our present prototype dimensions to a real plasma lens pulsed in any external circuit. The plasma lens for $\bar{p}$-collection will have typically a length of 270 mm and an inner diameter of 190 mm.

2. Dynamic pinch model

We assume that when discharging a condenser bank into the quartz tube directly after a strong pre-ionization, the initial current conducting region is a cylindrical layer adjacent to the discharge tube wall. Then the layer starts to implode towards the axis and sweeps up all the particles it encounters on its travel. Thus we can suppose that the imploding plasma is a well-defined cylindrical layer enclosed between an inner boundary at radius r_i (shock front) and an external boundary with radius r_e, the so-called "magnetic piston", as shown in Fig. 1:

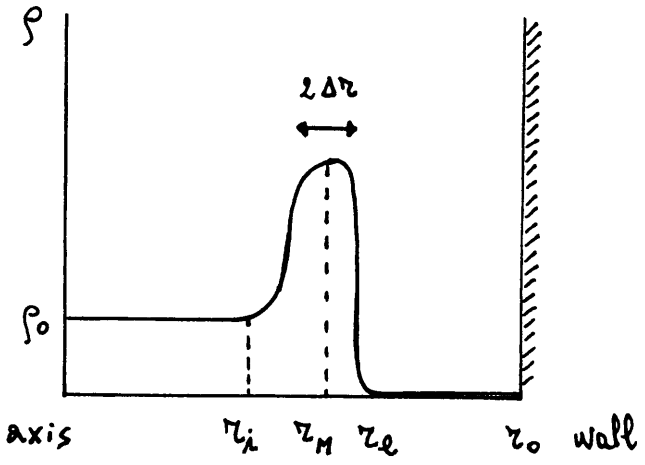

Figure 1 - Imploding plasma shell.

Furthermore we assume that the plasma distribution is cylindrically symmetric and infinite in length, so that all quantities depend only on the radius r and the time t.

In this section we describe the implosion phase of the z-pinch utilizing two quantities averaged over the layer region. We define the averaged quantities

$$r_M = \frac{2\pi \int(\rho\, r) r\, dr}{2\pi \int \rho\, r\, dr}$$

and

$$r_E^2 = \frac{2\pi \int(\rho\, r^2) r\, dr}{2\pi \int \rho\, r\, dr} ,$$

where the integrations are carried out over the layer region and ρ is the plasma mass density. Those quantities have a clear physical meaning:

i) r_M is the radius of the mass center of the plasma layer;

ii) $r_E^2 = r_M^2 + \Delta r^2$, where Δr is the plasma mass density dispersion width of the layer which is a measure of the layer thickness. r_E is the mean-square radius of the layer, which is always larger than r_M and closer to r_e than r_M. If $\Delta r = 0$, i.e. the layer is infinitesimally thin, then $r_M = r_E$. We assume the following boundary conditions on both sides of the layer:

- The mass density ρ is equal to the initial density ρ_0 inside the inner boundary and is equal to zero outside the magnetic piston.

- The kinetic pressure p is equal to the initial pressure p_0 inside the inner boundary and equal to zero outside the magnetic piston.

- The plasma velocity is equal zero inside the inner boundary and equal to the magnetic piston velocity inside the layer.

- The magnetic field B_ϕ, purely poloidal, is equal to zero inside the inner boundary and given on the external boundary by

$$B_\phi(r=r_e) = \frac{\mu_0\, i_p}{2\pi\, r_e} ,$$

where i_p is the total plasma current flowing in the layer.

- The heat flow and the conductivity are equal to zero outside the layer.

2.1 Snow-plow momentum equation and snow-plow energy equation for the z-pinch

T. Miyamoto[4] has obtained the equations for r_M and r_E in a consistent way, assuming that the plasma layer is thin compared with the averaged radii r_M and r_E and neglecting the first order terms of the layer thickness Δr. With the specific heat ratio $\gamma = 2$ these equations are

$$\frac{d}{dt}\left[M_M \frac{dr_M}{dt}\right] = -2\pi(p^*_{eM} - p^*_{iM})r_M \,, \tag{1}$$

$$\frac{d}{dt}\left\{\frac{1}{4}\frac{d}{dt}\left[M_E \frac{dr_E^2}{dt}\right] + \pi(p^*_{eE} - p^*_{iE})r_E^2\right\} = -2\pi\, p^*_{eE} r_E \frac{dr_E}{dt} - 2\pi\, p^*_{iE} r_E \frac{dr_E}{dt} \,, \tag{2}$$

where

$$p^* = p + B_\phi^2/2\mu_0,$$

$$p^*_{eM} = p^*_e(r_e=r_M), \qquad p^*_{iM} = p^*_i(r_i=r_M),$$

$$p^*_{eE} = p^*_e(r_e=r_E), \qquad p^*_{iE} = p^*_i(r_i=r_E).$$

and M_M, M_E are the total mass per unit length of the layer, neglecting all higher order terms of Δr, as functions of r_M and r_E. If t_a is the time in which the inner boundary arrives at the axis, M_M and M_E may be written as

$$M_M = \begin{cases} \pi \rho_0 (r_0^2 - r_M^2) & t < t_a \\ \pi \rho_0 r_0^2 & t \geq t_a \end{cases} \tag{3}$$

and

$$M_E = \begin{cases} \pi \rho_0 (r_0^2 - r_E^2) & t < t_a \\ \pi \rho_0 r_0^2 & t \geq t_a \,, \end{cases} \tag{4}$$

where r_0 is the inner radius of the discharge tube.

In our case p^*_{eM} and p^*_{iE} are equal to the initial pressure p_0, while p^*_{eM} and and p^*_{eE} are given by:

$$p^*_{eM} = \frac{1}{2\mu_0}\left(\frac{\mu_0 i_p}{2\pi r_M}\right)^2 \,, \tag{5}$$

$$p^*_{eE} = \frac{1}{2\mu_0}\left(\frac{\mu_0 i_p}{2\pi r_E}\right)^2 \,, \tag{6}$$

Equation (1) shows the balance of the radial component of the linear momentum. It may be derived from the one-fluid MHD equations[5]. This equation is just the so-called "snow-plow equation" which Miyamoto calls the "snow-plow momentum" equation (the SPM equation). It has been derived by Rosenbluth et al.[6].The right-hand and left-hand sides of eq. (1) simply express the external and inertia forces at zero-order in the layer thickness Δr.

Equation (2) shows the law of conservation of energy. The left-hand side of this equation represents the change of total energy stored in the layer per time unit while the first term on the right-hand side is the work per time unit done by the magnetic piston and the second term is the flux of internal energy through the inner boundary of the layer. This equation may also be derived from the one-fluid MHD equations using the law of conservation of energy[5]. The left-hand side of eq. (2) includes the contribution of internal energy in the layer which is neglected in the SPM equation[4]. Miyamoto calls this equation "snow-plow energy" equation (the SPE equation).

The SPM and SPE equations cannot give the time t_a. An approximate measure of this time is the moment in which the acceleration changes its sign from negative to positive value during the implosion phase. This means that the layer begins to decelerate when its inner boundary arrives on the axis.

The SPE equation gives a more realistic solution than the SPM equation up to the time of the first pinch contraction because this equation includes the contribution of the internal energy of the layer. It predicts a finite radius at the time of the first contraction, whereas the SPM equation gives zero radius. Furthermore the SPE equation describes, though only qualitatively, the observed plasma oscillations around the axis after the first contraction. In this note we shall examine the z-pinch dynamics only until the first contraction using the SPE equation.

Introducing the following non-dimensional parameters

$$x = \frac{r_E}{r_0}, \quad \tau = \frac{t}{t_c}, \quad \bar{i} = \frac{i_p t_c}{(4\pi^2 r_0^4 \rho_0/\mu_0)^{0.5}}, \tag{7}$$

where t_c is a characteristic time, using the eqs. (4) and (6) and remembering that $p^*_{iE} = p_0$, we rewrite eq. (2) as:

$$\frac{d^2}{d\tau^2}\left[(1 - x^2)\frac{dx^2}{d\tau}\right] = -4\left(\frac{\bar{i}}{x}\right)^2 \frac{dx^2}{d\tau} - 2x^2 \frac{d}{d\tau}\left(\frac{\bar{i}}{x}\right)^2 \tag{8}$$

for $\tau < \tau_a$ and

$$\frac{d^3x^2}{d\tau^3} = -4\left(\frac{\bar{i}}{x}\right)^2 \frac{dx^2}{d\tau} - 2x^2 \frac{d}{d\tau}\left(\frac{\bar{i}}{x}\right)^2 \tag{9}$$

for $\tau > \tau_a$.

A complete analysis of the plasma layer implosion requires the knowledge of the current as function of time and of the circuit parameters.

2.2 Circuit equation

Neglecting diffusive phenomena we can represent the z-pinch in the equivalent electrical circuit like a variable inductor with inductance L_p in series with a variable resistance R_p, as shown in Fig. 2.

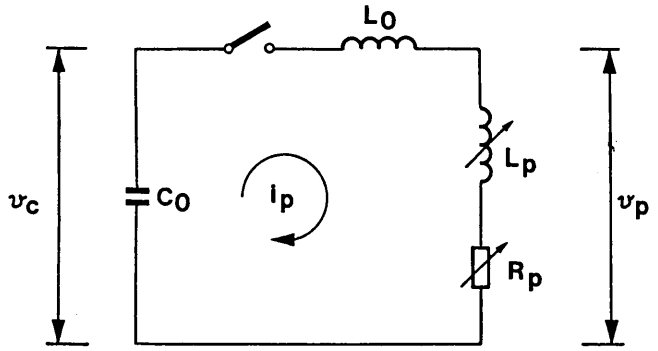

Figure 2 - Equivalent electrical circuit of z-pinch. C_0 = capacitance of the capacitor bank, L_0 = fixed external circuit inductance, υ_c (o) = V_0 = initial voltage across the capacitor bank.

We assume that the discharge current returns on a coaxial path which is a cylinder of radius R_0 just outside the walls of the discharge tube. Retaining only the zero-order term in layer thickness Δr, L_p may be represented by

$$L_p = \frac{\mu_0 \ell}{2\pi} \ln\left(\frac{R_0}{r_{0x}}\right) \tag{10}$$

where ℓ is the length of the discharge tube. We write the circuit equations as

$$\begin{aligned} \frac{d}{dt}\left[(L_p + L_0) i_p\right] + i_p R_p &= \upsilon_c \\ C_0 \frac{d\upsilon_c}{dt} &= -i_p \end{aligned} \tag{11}$$

Using eq. (10), the eqs. (11) may be rewritten as

$$\begin{aligned} \frac{di}{d\tau} &= \frac{(t_c V_0 / I_0 L_0)\bar{\upsilon}_c + \beta(i/x)(dx/d\tau) - \varepsilon i}{[1 + \beta(\delta - \ln x)]} \\ \frac{d\bar{\upsilon}_c}{d\tau} &= -\left(\frac{I_0 t_c}{V_0 C_0}\right) i \ , \end{aligned} \tag{12}$$

where we have chosen

$$i = \frac{i_p}{I_0} \ , \quad \bar{\upsilon}_c = \frac{\upsilon_c}{V_0} \ , \quad \beta = \frac{\mu_0 \ell / 2\pi}{L_0} \ , \quad \delta = \ln \frac{R_0}{r_0} \ , \quad \varepsilon = \frac{R_p}{L_0} t_c \ , \tag{13}$$

and I_0 is a characteristic current. The scaling parameter β is the ratio of the characteristic pinch inductance to the external circuit inductance. The parameter δ is negligible, if the thickness of the discharge tube is smaller than its inner radius. The normalized voltage, $\upsilon = \upsilon_p / V_0$, across the pinch tube is given by:

$$\upsilon = \left(\frac{L_0 I_0}{V_0 t_c}\right) \beta \left\{ (\delta - \ell n\, x) \frac{di}{d\tau} - \frac{i}{x} \frac{dx}{dt} \right\} + \left(\frac{I_0}{V_0} R_p\right) i \tag{14}$$

Defining the normalization constants as

$$I_0 = \frac{V_0}{(L_0/C_0)^{0.5}}, \qquad t_c = (L_0 C_0)^{0.5}$$

and introducing

$$t_p = \left(\frac{4\pi^2 r_0^4 \rho_0}{\mu_0 I_0^2}\right)^{0.5}, \qquad \alpha = \frac{t_c}{t_p},$$

we may rewrite the SPE equations (8) and (9) coupled with the circuit equation (12) as

$$\begin{aligned} \frac{d^2}{d\tau^2}\left[(1 - x^2)\frac{dx^2}{d\tau}\right] &= -4\left(\frac{\alpha i}{x}\right)^2 \frac{dx^2}{d\tau} - 2x^2 \frac{d}{d\tau}\left(\frac{\alpha i}{x}\right)^2 \qquad \text{for } \tau < \tau_a \\ \frac{d^3}{d\tau^3} x^2 &= -4\left(\frac{\alpha i}{x}\right)^2 \frac{dx^2}{d\tau} - 2x^2 \frac{d}{d\tau}\left(\frac{\alpha i}{x}\right)^2 \qquad \text{for } \tau > \tau_a \end{aligned} \tag{15}$$

$$\frac{di}{d\tau} = \frac{\bar{\upsilon}_c + \beta(i/x)(dx/d\tau) - \varepsilon i}{[1 + \beta(\delta - \ell n\, x)]}$$

$$\frac{d\bar{\upsilon}_c}{d\tau} = -i$$

and the normalized voltage υ across the pinch tube is given by

$$\upsilon = \beta\left\{ (\delta - \ell n\, x) \frac{di}{d\tau} - \frac{i}{x}\frac{dx}{d\tau} \right\} + \varepsilon i \tag{16}$$

where now the scaling parameter ε is the ratio of the internal pinch resistance to the external circuit impedance.

$$\varepsilon = \frac{R_p}{(L_0/C_0)^{0.5}} \,. \tag{17}$$

The other scaling parameter α is the ratio of the characteristic capacitor discharge time t_c and the characteristic pinch time t_p.

The normalized initial conditions are

$$x(0) = 1, \quad \left.\frac{dx}{d\tau}\right|_0 = 0, \quad \left.\frac{d^2x}{d\tau^2}\right|_0 = 0, \quad \bar{v}_c(0) = 1, \quad i(0) = 0 \ . \tag{18}$$

2.3 Sinusoidal current

When $\beta \to 0$, i.e. $L_0 \gg \mu_0/2\pi$, the plasma current is almost sinusoidal. We shall examine this case now.

Assuming

$$i_p(t) = I_0 \sin\left(\frac{\pi}{2}\frac{t}{t_0}\right), \tag{19}$$

where

$$I_0 = \frac{V_0}{(L_0/C_0)^{0.5}}, \quad t_0 = \frac{\pi}{2}(L_0C_0)^{0.5} \ . \tag{20}$$

We may rewrite the SPE equations (8) and (9) as

$$\frac{d^2}{d\tau^2}\left[(1 - x^2)\frac{dx^2}{d\tau}\right] = -4\left[\frac{\lambda \sin(\tau/\lambda)}{x}\right]^2 \frac{dx^2}{d\tau} - 2x^2\left[\frac{d}{d\tau}\left(\frac{\lambda \sin(\tau/\lambda)}{x}\right)^2\right] \tag{21}$$

for $\tau < \tau_a$, and

$$\frac{d^3}{d\tau^3}x^2 = -4\left[\frac{\lambda \sin(\tau/\lambda)}{x}\right]^2 \frac{dx^2}{d\tau} - 2x^2\left[\frac{d}{d\tau}\left(\frac{\lambda \sin(\tau/\lambda)}{x}\right)^2\right] \tag{22}$$

for $\tau \geq \tau_a$, with the normalized initial conditions

$$x(0) = 1, \quad \left.\frac{dx}{d\tau}\right|_0 = 0, \quad \left.\frac{d^2x}{d\tau^2}\right|_0 = 0 \ . \tag{23}$$

Now the characteristic time t_c is given by

$$t_c = \left(\frac{4\pi^2 r_0^4 \rho_0}{\mu_0 (di_p/dt)_0^2}\right)^{0.25} \tag{24}$$

and the scaling parameter is $\lambda = t_0/(\pi \cdot t_c/2)$.

The characteristic time t_c is the normalization factor introduced by Rosenbluth et al.[6] into the "snow-plow model". It is easy to show, that, when $\lambda \to \infty$, i.e. $t_0 \gg t_c$, we obtain the case with a linearly rising current.

2.4 Computation procedure

We have numerically solved eqs (15) with the initial conditions (18) and eqs (21), (22) with the initial conditions (23) using the "SCEPTRE PROGRAM" (CERN COMPUTER LIBRARY)[7], a program for circuit analysis.

Introducing the following state variables

$$u = \frac{dx}{d\tau}, \qquad a = \frac{du}{d\tau} \tag{25}$$

with u = normalized velocity and a = normalized acceleration, we can rewrite the eqs (15) with the initial conditions (18) as

$$\begin{aligned} \frac{dx}{d\tau} &= u \\ \frac{du}{d\tau} &= a \\ \frac{da}{d\tau} &= f(x,u,a,\bar{v}_c,i) \\ \frac{d\bar{v}_c}{d\tau} &= -i \\ \frac{di}{d\tau} &= g(x,u,\bar{v}_c,i) \end{aligned} \tag{26}$$

$$x(0) = 1, \quad u(0) = 0, \quad a(0) = 0, \quad \bar{v}_c(0) = 1, \quad i(0) = 0 \tag{27}$$

where

$$g(x,u,\bar{v}_c,i) = \frac{\bar{v}_c + \beta(i/x)u - \varepsilon i}{[1 + \beta(\delta - \ln x)]} \tag{28}$$

$$f(x,u,a,\bar{v}_c,i) = \left\{6xu^3 - 3ua(1 - 3x^2) - 4\frac{(\alpha i)^2 u}{x} + 2\alpha^2 i \frac{iu - xg(x,u,\bar{v}_c,i)}{x}\right\}/[x(1 - x^2)] \tag{29}$$

for $\tau < \tau_a$ and

$$f(x,u,a,\bar{v}_c,i) = \left\{-3ua - 4\frac{(\alpha i)^2 u}{x} + 2\alpha^2 i \frac{iu - xg(x,u,\bar{v}_c,i)}{x}\right\}/x \tag{30}$$

for $\tau > \tau_a$.

In the same way we can rewrite the eqs (21) and (22) for sinusoidal current with the initial conditions (23) as:

$$\frac{dx}{d\tau} = u$$

$$\frac{du}{d\tau} = a \tag{31}$$

$$\frac{da}{d\tau} = f(x,u,a)$$

$$x(0) = 1, \quad u(0) = 0, \quad a(0) = 0 \tag{32}$$

where now $f(x,u,a)$ is given by:

$$f(x,u,a) = \left\{ 6xu^3 - 3ua(1 - 3x^2) - 4\,\frac{[\lambda \sin(\tau/\lambda)]^2 u}{x} + 2\lambda^2 \sin(\tau/\lambda)\,\frac{u \sin(\tau/\lambda) - x\cos(\tau/\lambda)/\lambda}{x} \right\} / [x(1 - x^2)] \tag{33}$$

for $\tau < \tau_a$ and

$$f(x,u,a) = \left\{ -3ua - \frac{[\lambda \sin(\tau/\lambda)]^2 u}{x} + 2\lambda^2 \sin(\tau/\lambda)\,\frac{u \sin(\tau/\lambda) - x\cos(\tau/\lambda)/\lambda}{x} \right\} / x \tag{34}$$

for $\tau > \tau_a$.

We consider now the set of general, non-linear, first order differential equations

$$\frac{dy_1}{dt} = f_1(y_1, y_2, \ldots, y_N, t)$$

$$\frac{dy_2}{dt} = f_2(y_1, y_2, \ldots y_N, t) \tag{35}$$

$$\ldots\ldots\ldots\ldots\ldots\ldots\ldots\ldots$$

$$\frac{dy_N}{dt} = f_N(y_1, y_2, \ldots, y_N, t)\ ,$$

with the initial conditions

$$y_1(t_0) = y_{10}, \quad y_2(t_0) = y_{20}, \ \ldots, \ y_N(t_0) = y_{NO} \tag{36}$$

and we illustrate two separate methods for applying SCEPTRE to physical systems which are not necessarily electrical ones. One method for solving non-electrical problems described by the eqs (35) with the initial conditions (36) consists in representing the eqs (35) by the equivalent circuits, shown in Fig. 3,

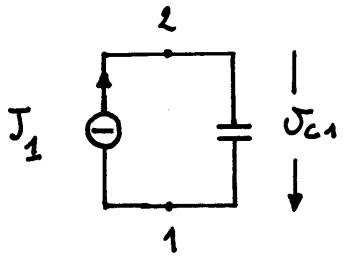

$J_1 = f_1(v_{C1}, v_{C2}, \ldots, v_{CN}, t), \quad v_{C1}(t_0) = y_{10}$

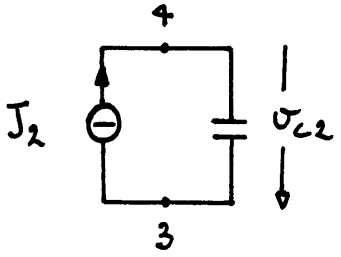

$J_2 = f_2(v_{C1}, v_{C2}, \ldots, v_{CN}, t), \quad v_{C2}(t_0) = y_{20}$

.....

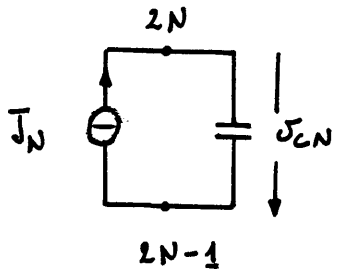

$J_N = f_N(v_{C1}, v_{C2}, \ldots, v_{CN}, t), \quad v_{CN}(t_0) = y_{NO}$

Figure 3 - Equivalent circuits for solving non-electrical problems with the SCEPTRE Program.

where the symbols $\oplus$ indicate current sources. All capacitance values are assumed to be equal to one. After conversion of all state variables into electrical quantities the SCEPTRE program is written for the equivalent circuit (Fig. 3) as follows:

```
CIRCUIT DESCRIPTION

(comments)

C1, 2-1 = 1
C2, 4-3 = 1
.....
CN, 2N-2N-1 = 1

J1, 1-2 = EQUATION 1 (VC1, VC2, ..., VCN, TIME)
J2, 3-4 = EQUATION 2 (VC1, VC2, ..., VCN, TIME)
.....
JN, (2N-1)-2N = EQUATION N (VC1, VC2, ..., VCN, TIME)
```

```
DEFINED PARAMETERS

OUTPUTS

INITIAL CONDITIONS

VC1 = Y10
VC2 = Y20
.........
VCN = YNO

FUNCTIONS

EQUATION 1 (VC1, VC2, ..., VCN, TIME)
           = (f1(VC1,VC2, ..., VCN, TIME))
EQUATION 2 (VC1, VC2, ..., VCN, TIME)
           = (f2(VC1, VC2, ..., VCN, TIME))
.........................................
EQUATION N (VC1, VC2, ..., VCN, TIME)
           = (fN,(VC1, VC2, ..., VCN, TIME))

RUN CONTROLS

    END
```

The second method uses the DEFINED PARAMETER mode as follows:

```
CIRCUIT DESCRIPTION

(comments)

DEFINED PARAMETERS

DPY1 = X1 (f1 (PY1, PY2, ..., PYN, TIME))
DPY2 = X2 (f2 (PY1, PY2, ..., PYN, TIME))
.........................................
DPYN = XN (fN (PY1, PY2, ..., PYN, TIME))

PY1 = Y10
PY2 = Y20
.........
PYN = YNO

OUTPUTS

RUN CONTROLS

    END
```

Notice that now the initial conditions for Y_1, Y_2, ..., Y_N are not entered under the INITIAL CONDITIONS subheading.

2.5 Numerical results

Now we present some results obtained with the SPE equation coupled to the circuit equations. When $\beta \ll 1$, the pinch current is almost sinusoidal. This happens when the external inductance is larger than the pinch inductance. When $a \simeq 1.1$ the first minimum pinch radius occurs when the current is at its maximum value, while when $a < 1.1$ it occurs after the maximum value of the current. When $a > 1$ the pinch phase occurs before the maximum value of the current and if $a \gg 1.1$ the pinch operates in the early part of a sinusoidal current, corresponding to the well known "snow-plow" case.

In Fig. 4 the computed results of x, i and υ for three sets of scaling parameters are shown, neglecting the ohmic losses in the plasma. In all three cases the very first stage of the process is characterized by an increase of the pinch inductance due to the contraction of the plasma. The contraction speed increases with a, hence increases with the initial voltage on the capacitor bank and decreases with the initial pressure p_0. At the moment of the first full contraction of the plasma column, a kink appears on the current waveform. The first peak of the voltage waveform, during the implosion phase, occurs when the velocity is at its maximum value. After the steep rise a sharp drop appears on the voltage waveform when the plasma contraction velocity comes to zero and changes sign. We call the moment of minimum pinch radius, which coincides with the zero crossing of the voltage and the kink in the current waveform, the characteristic pinch time $t_{pinch} = \tau_{pinch} \cdot t_c$. The contraction phase is followed by a rapid expansion of the plasma column. We have also solved the SPE equation with sinusoidal current. In Fig. 5 we show the normalized pinch current $i(\tau_p)$ and the normalized pinch time τ_p as function of the scaling parameter λ. For $\lambda = 1.1$ the first minimum pinch radius occurs when the current is at its maximum value, while for $\lambda < 1.1$ it occurs later and for $\lambda > 1.1$ it occurs before. When $\lambda \to \infty$ the pinch happens in the early linear part of the sinusoidal current and we find $\tau_p = 1.55$. The same value was found by Rosenbluth, solving the "snow-plow equation", and by Miyamoto, solving the SPE equation, with a linearly rising current. When $\lambda \to \infty$, $i(\tau_p)$ can be approximated by $1.55/\lambda$.

3. Experimental set-up

Figure 6 shows the experimental set-up for voltage, current and field distribution measurements in the plasma lens prototype II. The capacitor bank of 281 µF capacity can be charged up to 12kV corresponding to a maximum stored energy of 20kJ. A triggered high current switch transfers the electrical power to the plasma lens via a 35 cm wide stripline. The total circuit inductivity is around 750 nH mainly because of the high internal condenser inductance. This results in a full current cycle wavelength of 90 µs. The discharge is generated inside a cylindrical quartz tube of 236 mm inner diameter, 7 mm wall thickness and 250 mm length (plasma lens prototype II). The two hollow electrodes are made of stainless steel each with a 25 mm diameter centre hole. The current leads between the stripline and the lens electrodes are made by 18 copper bolts. The quartz tube volume is normally filled with argon or helium at low pressure (0.05 to 5 mbar). A weak preionisation of 1 mA (5kV) is applied to the plasma lens via a 10 MΩ resistor. The differential voltage across the lens is measured by two commercial high voltage probes. "Top" and "bottom" signals are both fed into a differential amplifier. The total current through the lens is measured with Rogowsky coils.

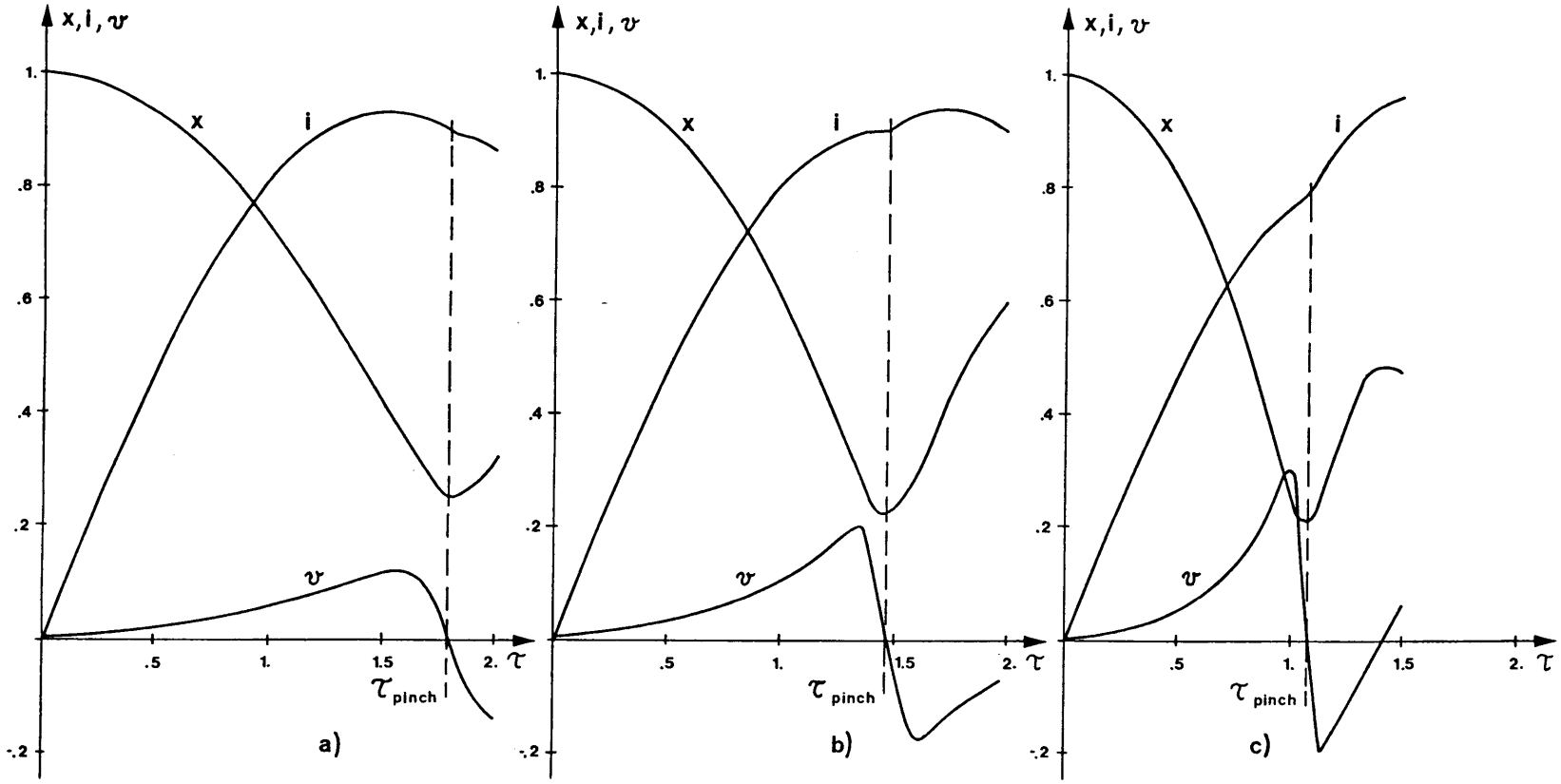

Figure 4 - Computation of normalized plasma column radius x, normalized current i and normalized voltage υ as functions of normalized time τ with the general SPE model for three sets of scaling parameters.

a) $\beta = 5/70$, $\alpha = 0.9$ (Argon, $p_0 = 1$ mbar, $V_0 = 10$ kV).
b) $\beta = 5/70$, $\alpha = 1.3$ (Helium, $p_0 = 5$ mbar, $V_0 = 10$ kV).
c) $\beta = 5/70$, $\alpha = 2.3$ (Argon, $p_0 = 0.16$ mbar, $V_0 = 10$ kV).

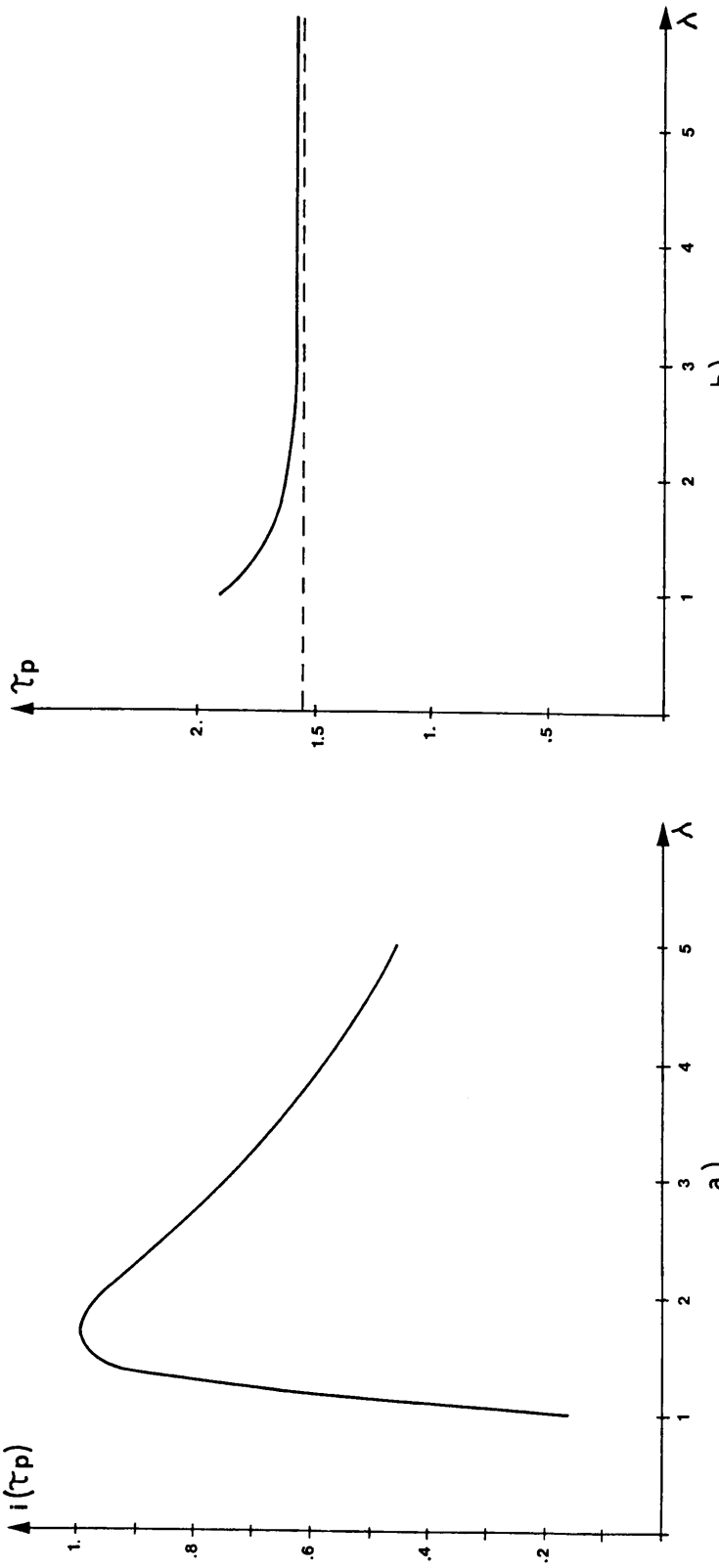

Figure 5 - a) Computed normalized current i at the normalized pinch time τ_p and
b) Normalized pinch time τ_p as function of $\lambda = 2t_0/\pi\ t_c$ in the case of sinusoidal current (external circuit inductance $\gg L_p$).

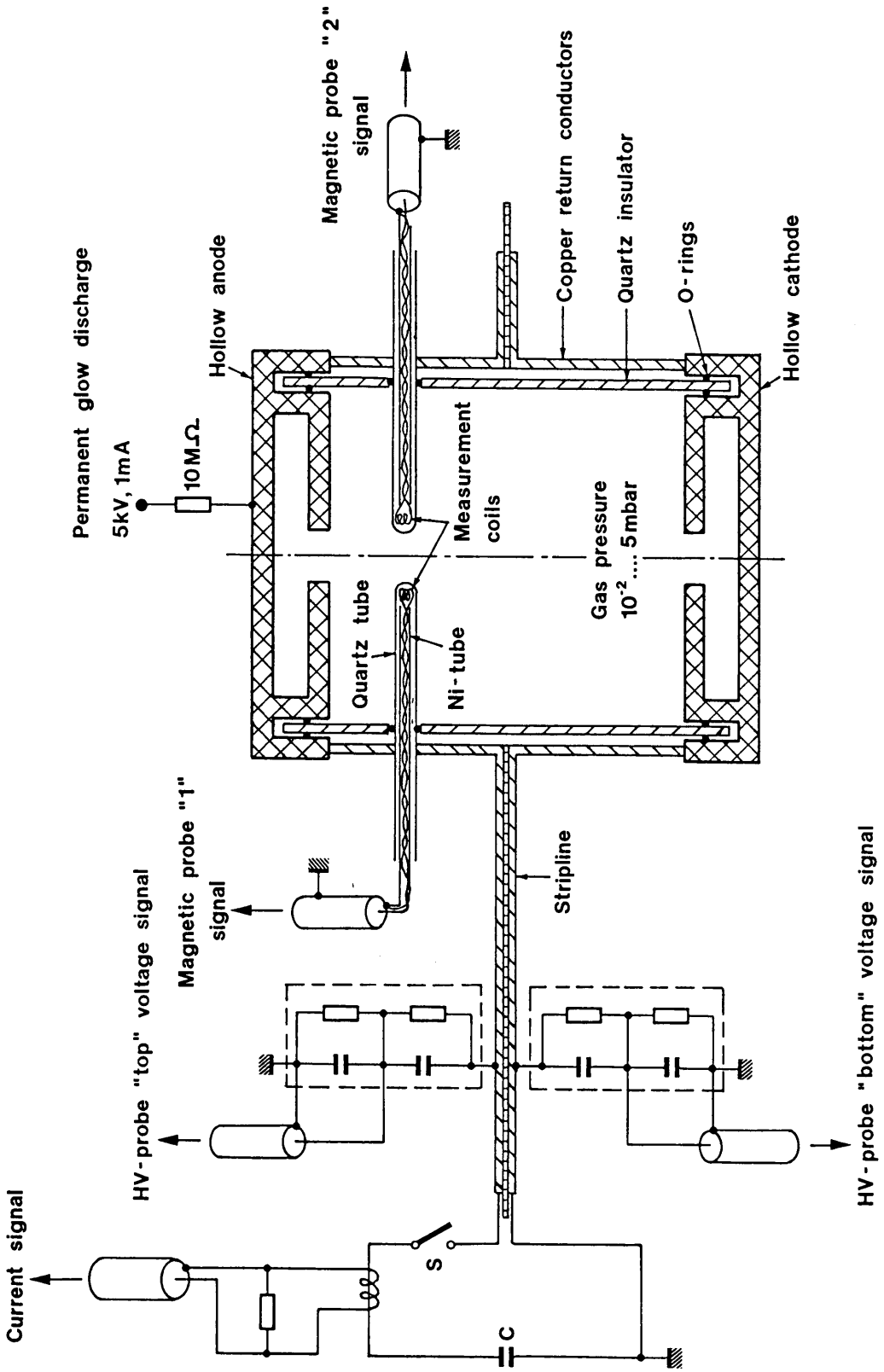

Figure 6 - Scheme of plasma lens prototype II with pulse generator and measurement set-up.

Magnetic field and current density distributions as well as discharge symmetry inside the tube are measured with two magnetic probes inserted symmetrically to the axis from two opposite holes in the quartz tube wall. A magnetic probe consists of a 0.3 mm long coil of 25 turns with a diameter of 0.5 mm. The probes are protected against high frequency perturbations by a nickel tube of 2 mm diameter which is electrically connected to the Faraday cage earth. The coil itself is not completely covered by the nickel tube to avoid magnet field screening. Both probe systems are protected from the plasma either by one single 4 mm diameter quartz tube which traverses both holes in the plasma lens tube wall or each probe by a separate quartz tube closed up at the inside end. The latter arrangement was chosen to minimize the perturbation effects on the plasma discharge especially in the centre. With the present measurement system differences between both screening modes could not be detected. The coils can be moved together with the nickel screens inside the protecting quartz tubes. They can be fixed at any desired radius of the lens to measure the time variation of the magnetic field. Differential voltage, current and magnetic probe signals are triggered simultaneously with the main switch. While voltage and current signals are displayed directly on a storage oscilloscope, the two probe signals are digitized by two transient recorders with a sampling rate of 32 MHz (Fig. 7). The digitized signals can be displayed in analog form on an oscilloscope or be transferred to a CAVIAR computer system for further treatment. The probe signals are proportional to the derivative of the magnetic flux through the coils. Therefore the probe waveforms have to be integrated in time to show the magnetic field variation during the discharge. A data treatment programme in the CAVIAR controls via CAMAC the acquisition modules (attenuators, amplifiers, digitizers, etc) and collects and evaluates the data sets of magnetic field distribution measurements for different discharge parameters like gas pressure or charging voltage.

4. Experimental results

The pinch radius determines the magnetic field distribution which we need to know when applying a plasma lens device to high energy particle focalisation. The dependence on gas type and gas pressure, charging voltage, inner quartz tube radius, etc. has to be studied. For the prototype II plasma lens we have up to now gathered results of differential voltage and current measurements, as well as of magnetic field measurements, while for the original 40 mm diameter prototype I lens we have no magnetic field distribution results, but fast streak camera measurements together with voltage and current waveforms.

All voltage waveform measurements (Figs 8 to 11) show a typical concave rise up to a few kV with either one or more peaks followed by a sharp voltage drop. One can observe the preionisation potential of a few hundred volts in front of the pulse. After ignition the rising voltage signalizes increasing internal lens impedance. We expect this behaviour also from the collapse of the current sheet.

The current waveforms show a typical "kink" at the time of the voltage-peak also hinting to a major change of the internal lens impedance. Depending on the chosen parameters gas type, gas pressure and charging voltage the kink appears either before, after or just at the time of maximum current. In the latter case the current waveform shows a rather flat top and the peak current decreases. Reproducibility of consecutive pulses was tested by comparing the voltage signals of consecutive shots. Figure 12 shows some examples of reproducibility.

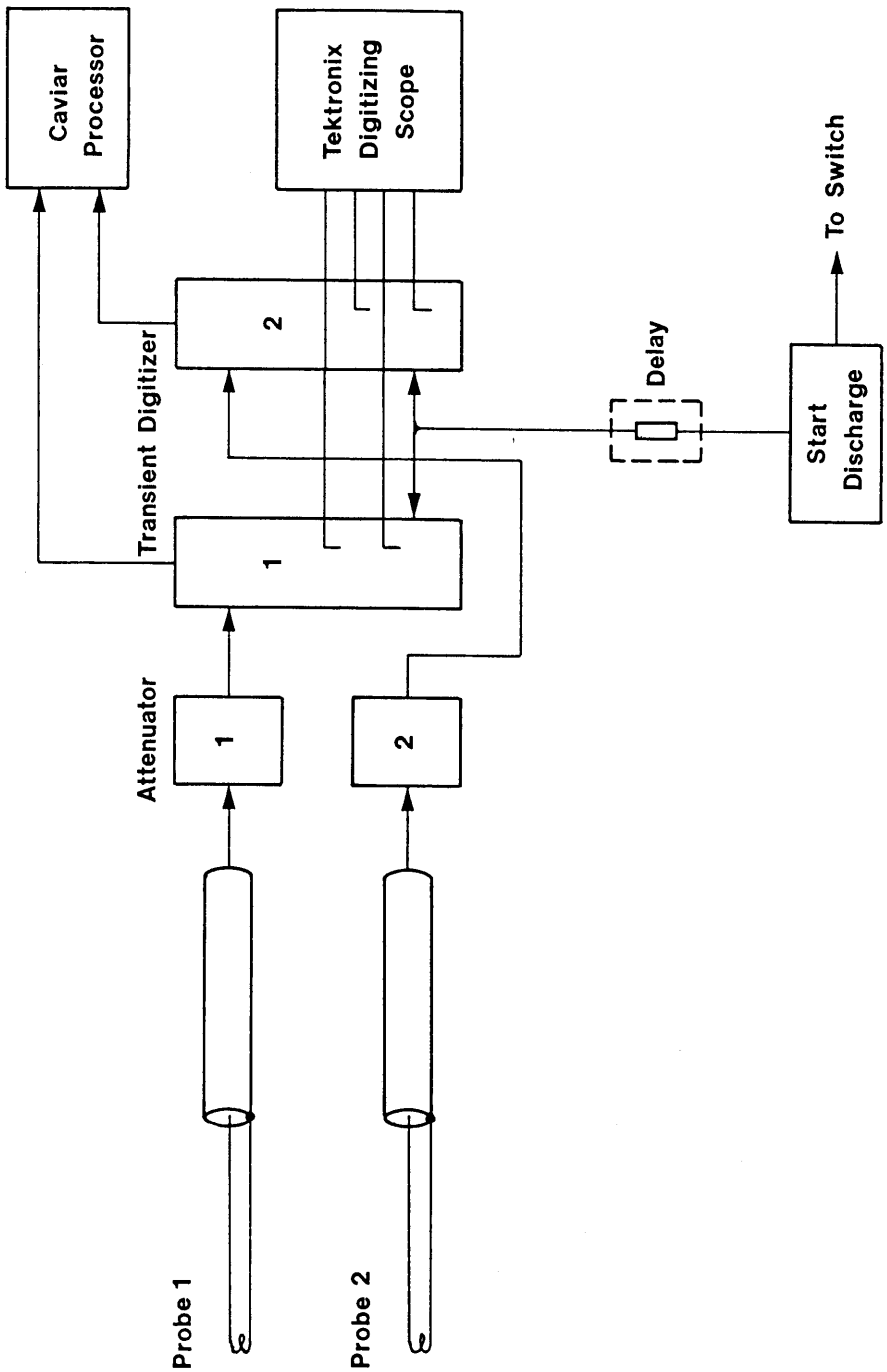

Figure 7 - Data acquisition and handling set-up for magnetic field distribution measurements.

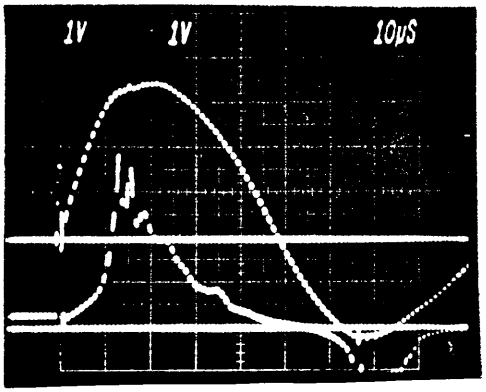

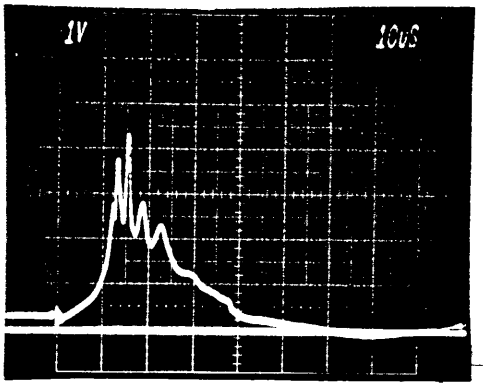

Figure 8

a) Current (upper) and voltage (lower) waveforms for 10 kV charging voltage with argon at 0.16 mbar.
Current : 37 kA/div.
Voltage : 1 kV/div.

b) Voltage waveform only for the same parameters.

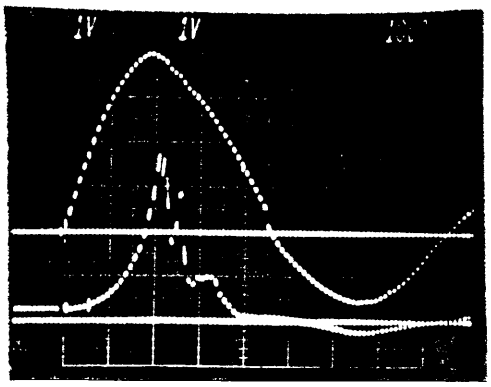

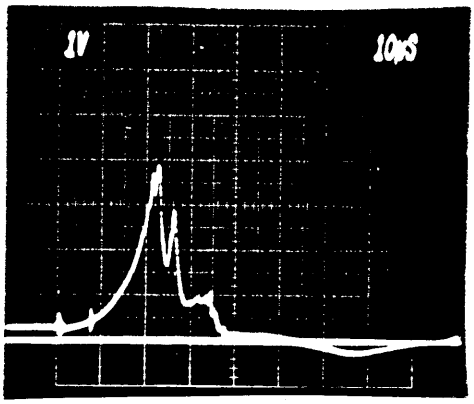

Figure 9

a) Current (upper) and voltage (lower) waveforms for 10 kV charging voltage with argon at 0.4 mbar.
Current : 37 kA/div.
Voltage : 1 kV/div.

b) Voltage waveform only for the same parameters.

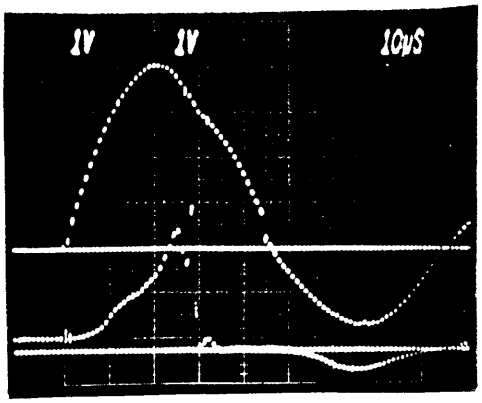

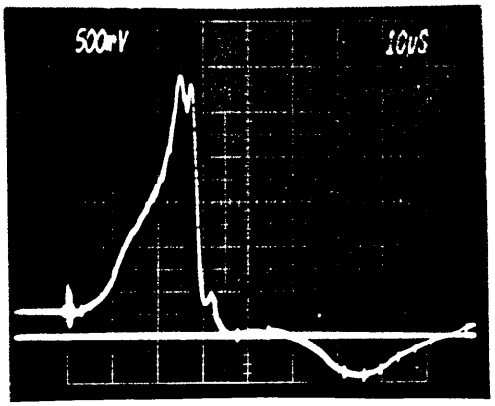

Figure 10

a) Current (upper) and voltage (lower) waveforms for 10 kV charging voltage with argon at 1 mbar.
Current : 37 kA/div.
Voltage : 1 kV/div.

b) Voltage waveform only for the same parameters.

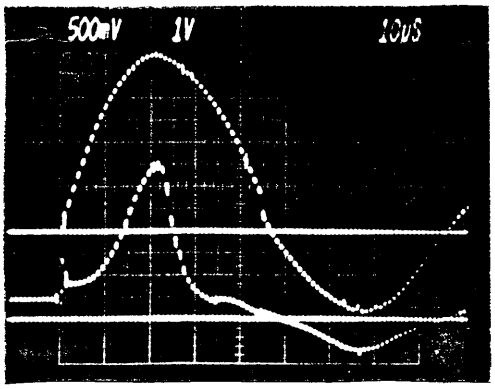

Figure 11 - Current (upper) and voltage (lower) waveforms for 10 kV charging voltage with helium at 5 mbar.
Current : 38.6 kA/div.
Voltage : 0.5 kV/div.

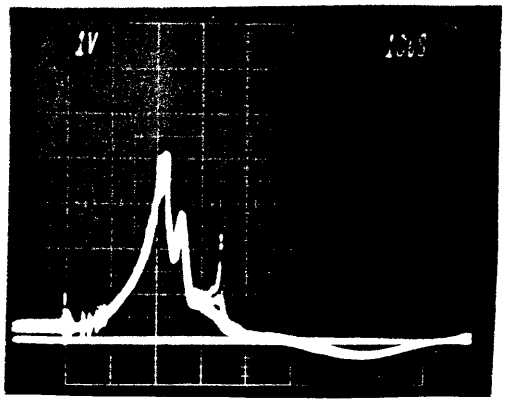

a) 0.4 mbar Ar, V_o = 10 kV

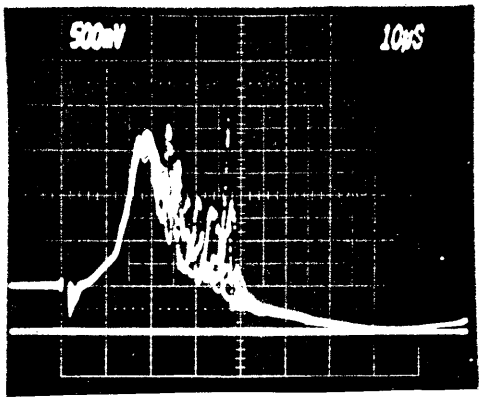

b) 0.07 mbar He, V_o = 6 kV

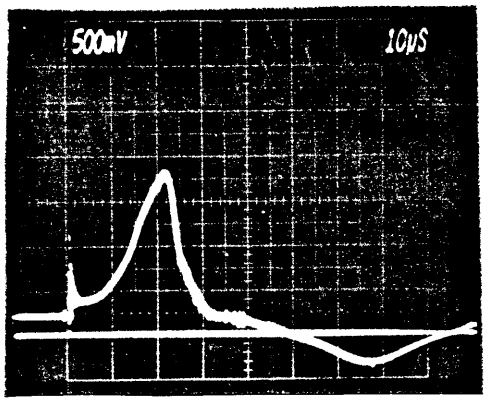

c) 5 mbar He, V_o = 10 kV

Figure 12 - Reproducibility of the discharge illustrated by superposition of 5 consecutive voltage waveforms for cases a), b) and c).
All voltage waveforms are reproducible for Ar and He up to the first peak. He shows instabilities below 0.1 mbar.

Figure 13 shows two typical signals simultaneously obtained from the same shot, with the two magnetic field pickup coils. Both probes are symmetrically placed at equal radii opposite to each other.

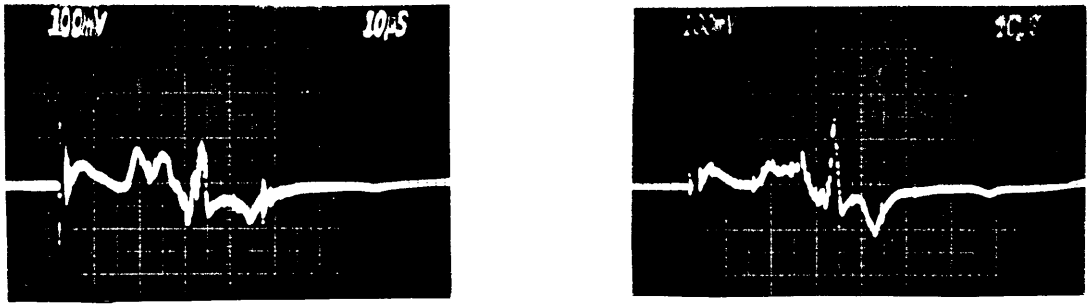

a) b)

Figure 13 - Magnetic probe signals for one shot obtained simultaneously with two probes a) and b) placed at equal radius of 60 mm for 0.02 mbar argon and 4 kV charging voltage. Vertical : 100 mV/div, horizontal : 10 μs/div.

With the symmetrical arrangement of both probes we can check the symmetry of the discharge. Both signals are identical up to the pinch phase. The plasma column decay afterwards is generally asymmetric.

Figure 14 shows the magnetic flux density at different radii for a charging voltage of 10 kV and a pressure of 0.4 mbar in argon as a function of time. The voltage and current waveform for this case is shown in Fig. 9.

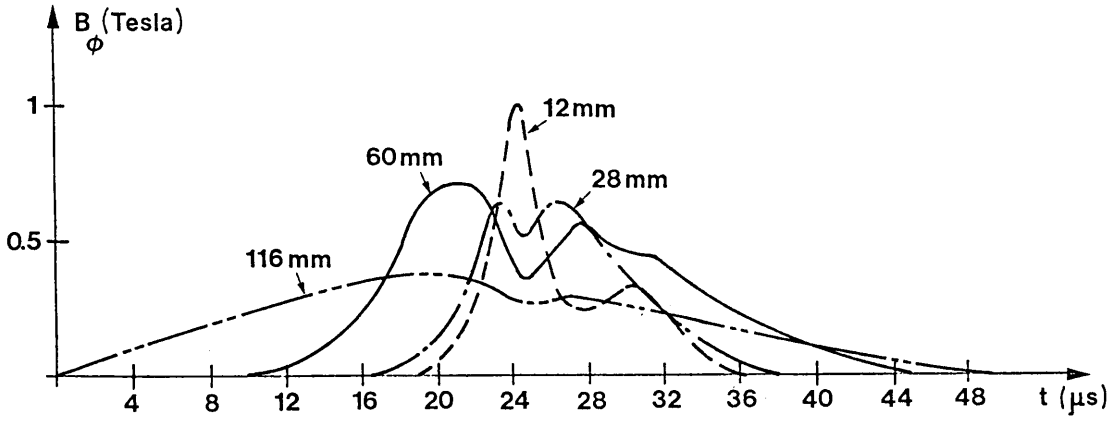

Figure 14 - Magnetic flux density B_ϕ as function of time after discharge at different radii. Charging voltage: 10 kV; pressure: 0.4 mbar Ar.

For large radii > 110 mm, the magnetic field waveform approaches the shape of the total current waveform through the plasma lens. The kink in the current waveform of Fig. 9 occurs at 25μs like in the flux density waveform (Fig. 14) at radius 116 mm. For radii, smaller than the pinch radius the field has a maximum at this time. Figure 15 is a plot of the measured magnetic flux density as a function of the radius.

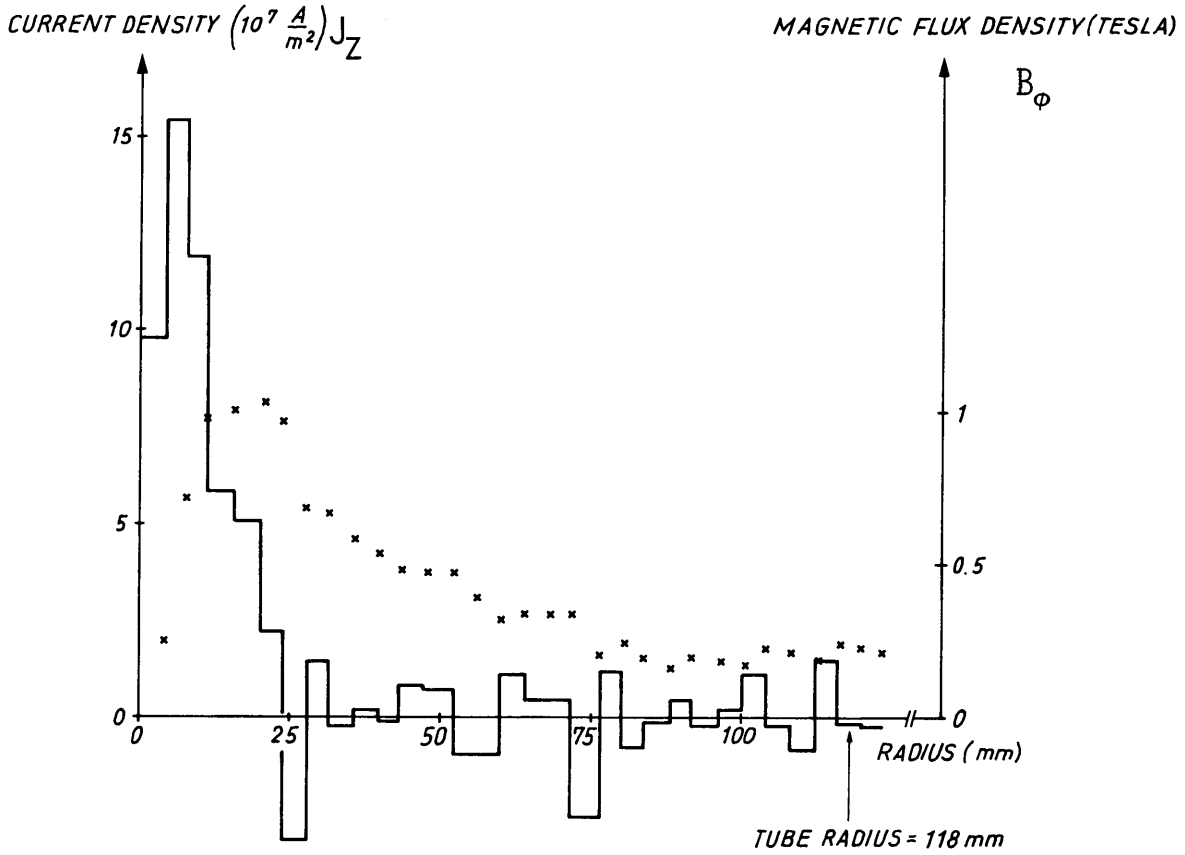

Figure 15 - Measured magnetic flux density B_ϕ and calculated current density J_z (according to eq. (37)) 25 μs after ignition as a function of radius. Charging voltage: 10 kV, pressure: 0.4 mbar Ar.

A rather linear rise up to about 1 Tesla at 12 mm radius is followed by an hyperbolic decay. The same figure shows the current density J_z calculated from the field distribution $B_\phi(r)$ assuming cylindrical symmetry, current flow only in z-direction and reproducibility of consecutive discharges, according to the formula:

$$J_z = \frac{1}{\mu_0}\left(\frac{B_\phi}{r} + \frac{\partial B_\phi}{\partial r}\right) . \qquad (37)$$

As the current density is not confined to an infinitely thin sheet, but is distributed, we define the pinch radius in Fig. 15, where the current density has dropped to about 1/e of its maximum value. At that time nearly all the current flows within a column of about 20 mm radius and the current density reaches values of 10^8 A/m^2. The corresponding voltage signal, after decreasing sharply, has a minimum at this time coinciding with the kink in the current wave form (see Fig. 9).

It is proven that the current always starts to flow near the inner quartz tube wall and the conducting current layer moves inward with an average velocity of the order of 1 cm/µs. Figure 16 shows the magnetic field as a function of radius for the same parameter values as in Fig. 15, but at 10 µs after the start of the pulse.

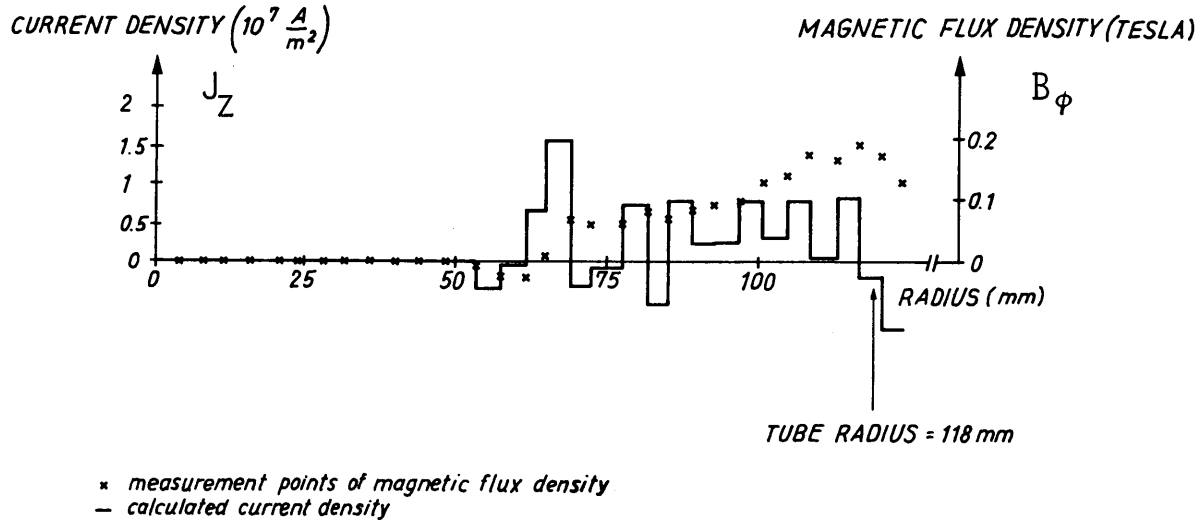

Figure 16 - Measured magnetic flux density B_ϕ and calculated current density J_Z as a function of radius 10 µs after ignition. Charging voltage: 10 kV, pressure: 0.4 mbar Ar.

The current density calculated from this field distribution proves that the current flows in a rather extended region and not in a very thin sheet. This behaviour is qualitatively observed for all parameter sets covered by the measurements.

5. Comparison of computations and experimental results

In this chapter we will present some selected examples of computational results with parameter sets which have also been applied in experimental tests. Detailed experimental results of field and current density distributions and of plasma compression dynamics, together with their matching to a suitable pinch model will be described in a later report. In this note the comparisons concern mainly current and voltage waveforms though, for the case of a charging voltage of 10 kV in argon at a pressure of 0.4 mbar, also the pinch radius and the pinch time have been determined as functions of time.

The concave voltage rise appears as well in the experiments with prototype lens II as in the SPE model. This is a prove that the ohmic resistance is negligible in the initial implosion phase. Figure 17 shows a typical voltage waveform measured on PL prototype II. Here it is useful to introduce two characteristic time values t_1 and t_{max}, as defined in Fig. 17, for comparisons of experimental results and computations. Sometimes both values may coincide, like in PL prototype I, and may be equal to the pinch time t_{pinch} (time of minimum plasma column radius). The latter coincides for prototype II with the sharp voltage drop after the peak. In Fig. 18 we see that the peak voltage increases with the initial charging voltage and decreases with pressure.

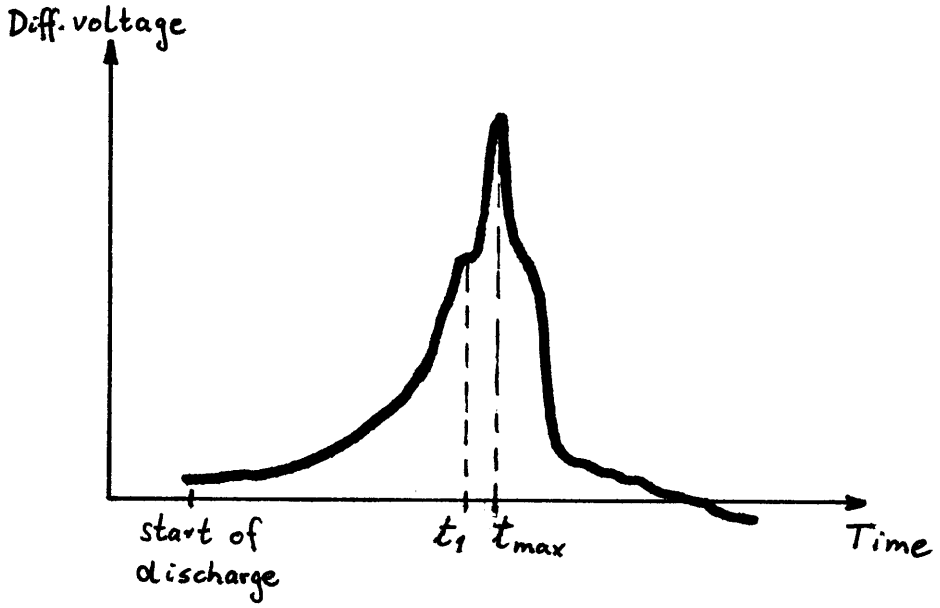

Figure 17 - Schematic drawing of a typical voltage waveform defining the characteristic times t_1 and t_{max}.

In Fig. 19 one can recognize that the characteristic times t_1 and t_{max} of the voltage waveform for 10 kV charging voltage increase with pressure until 1 mbar and decrease for higher pressure. This is also valid at charging voltages of 6kV, 8kV and 12 kV. We obtain good agreement between the computed and experimental waveforms in this respect. For pressures below 0.1 mbar the computed pinch time t_{pinch} and the voltage peak time t_{max} are close together but for pressures above 1 mbar the computed pinch time t_{pinch} is greater than t_{max} . Figure 20 shows also good agreement of the computed and measured characteristic time parameters as a function of the charging voltage. Above 1 mbar t_{pinch} increases with decreasing charging voltage while t_{max} increases down to 8 kV and decreases for lower values. Figure 21 is a plot of the lens current values at the characteristic times t_{pinch} and t_{max} as a function of the pressure. With higher pressure the current increases due to the shift of the charasteristic time values towards the maximum of the current wave. When the pinch and the kink coincide with the current maximum, the peak current decreases, especially at pressures above

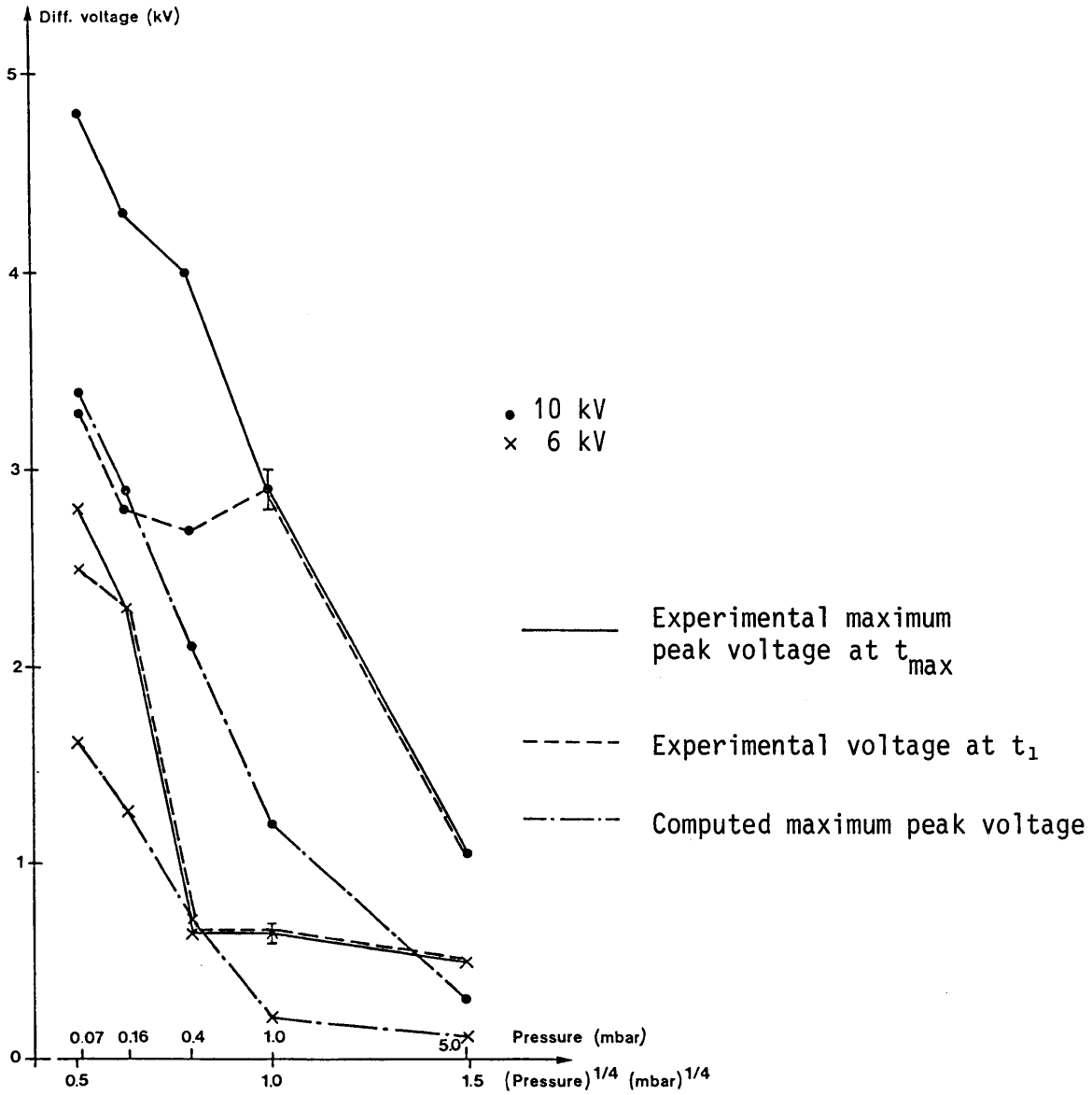

Figure 18 - Comparison of experimental and computed results of the plasma lens voltage as a function of gas pressure (Argon).

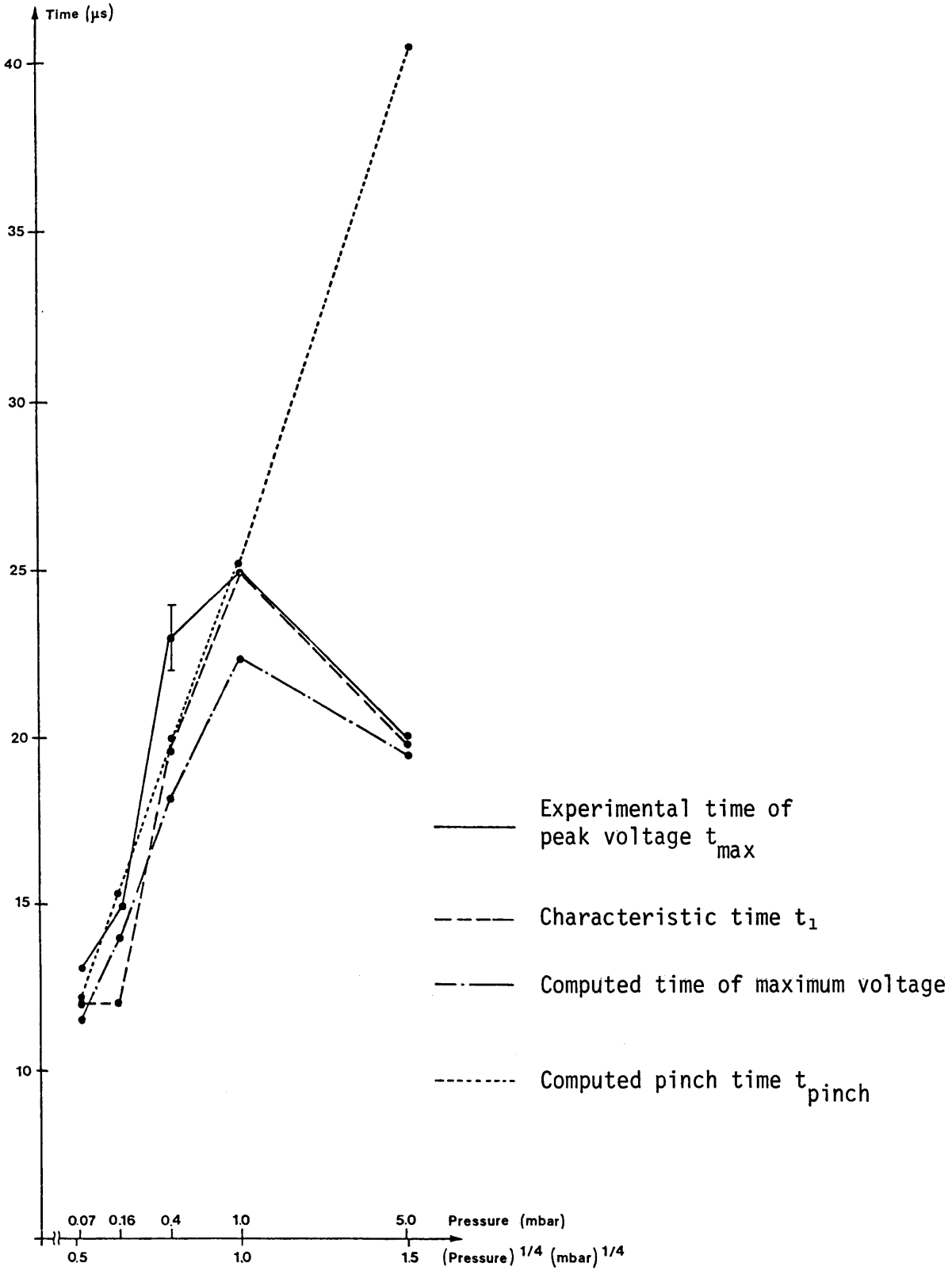

Figure 19 - Comparison of experimental and computed results of the characteristic time values of the voltage across the plasma lens as a function of Argon gas pressure. V_o = 10 kV.

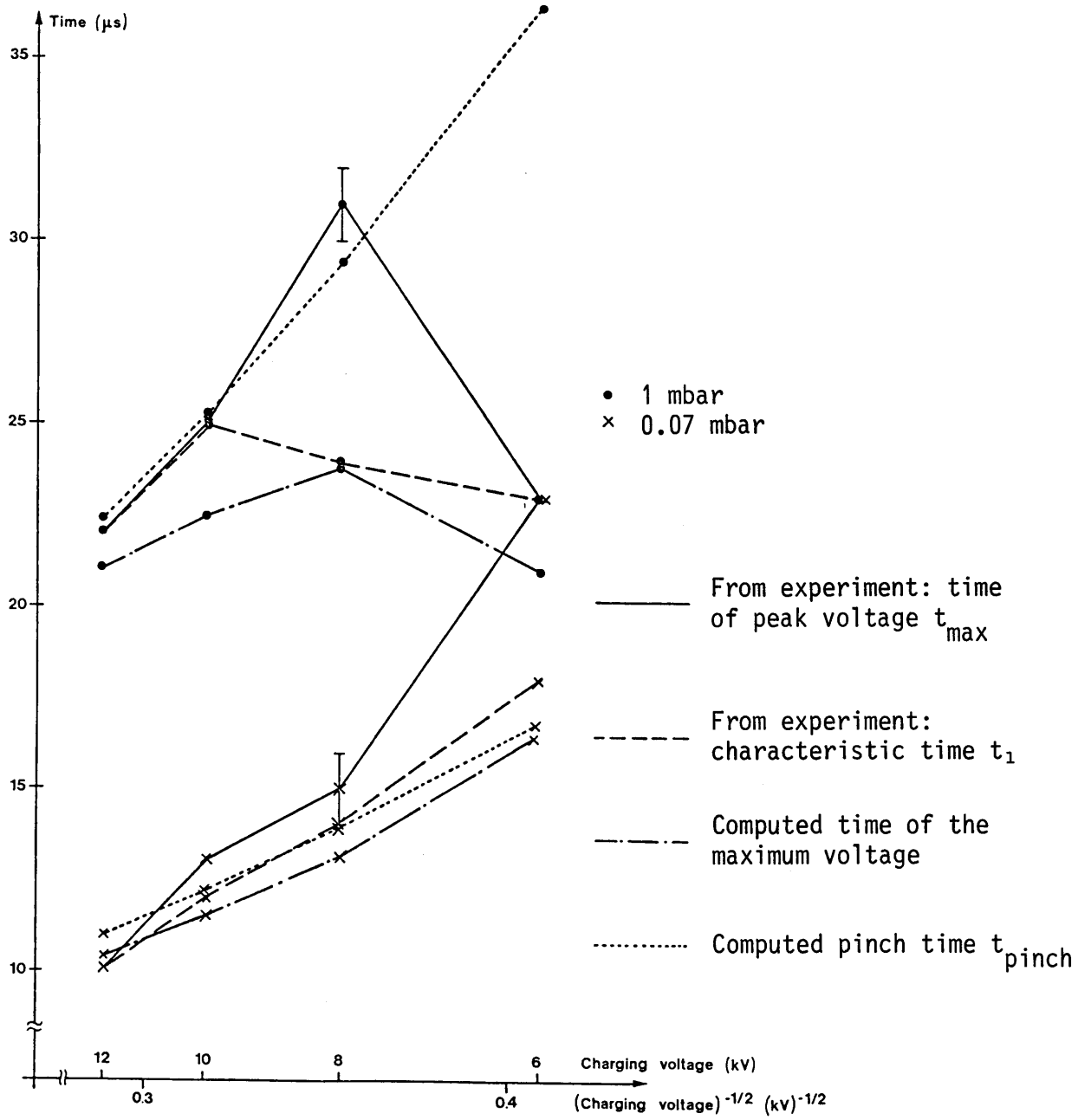

Figure 20 - Comparison of experimental and computed results of the characteristic time values of the voltage waveform as a function of charging voltage at 0.07 and 1 mbar in argon.

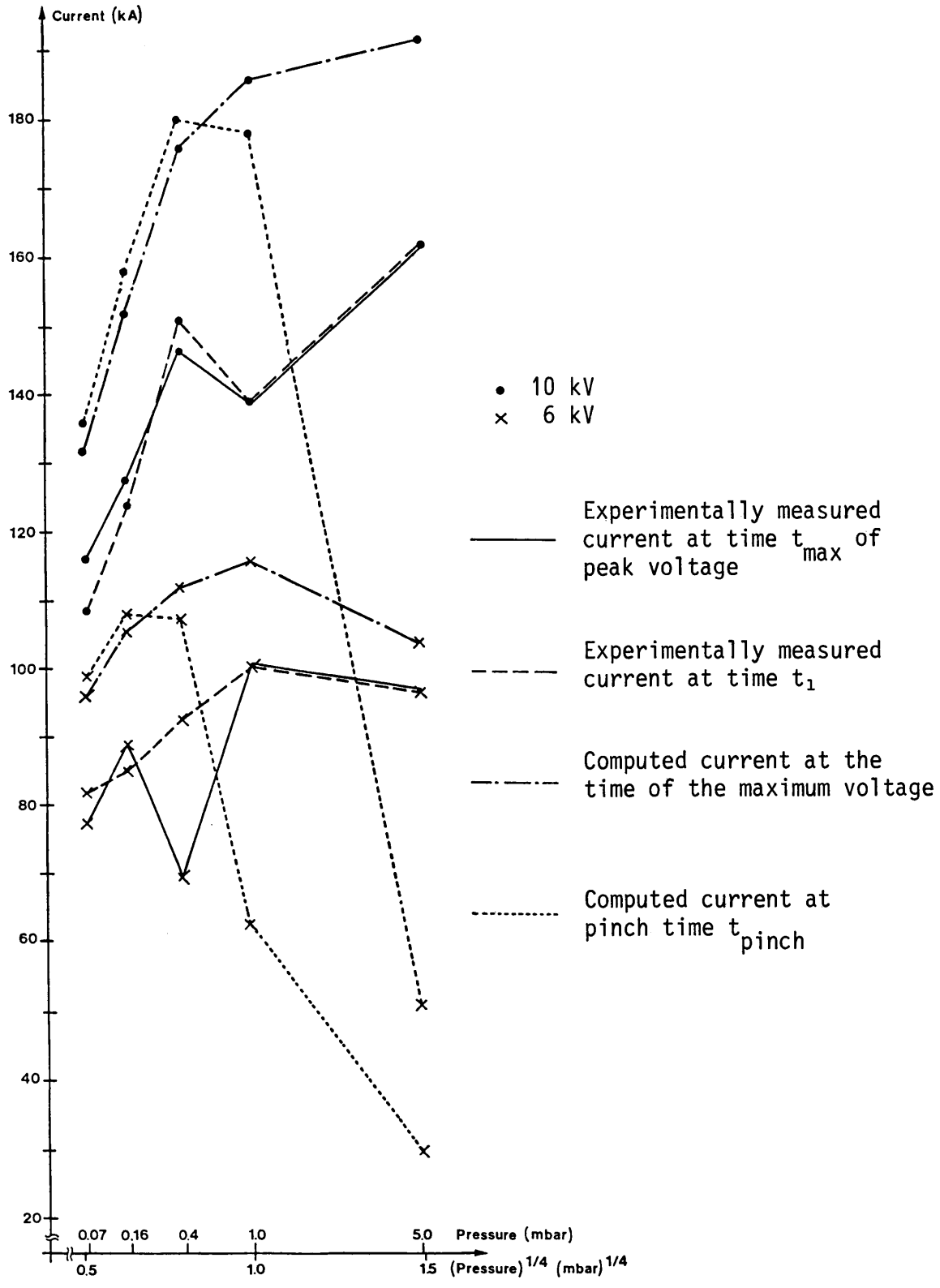

Figure 21 - Comparison of experimental and computed results of the plasma lens current at different characteristic times of the pinching process as a function of gas pressure (Argon).

1 mbar. However, a difference of about 20% appears between the experimental and numerical results. The computed current at the pinch time t_{pinch} with 5 mbar is lower than the experimentally observed current at the characteristic times because the computed pinch time is more than 40 μs (see Fig. 19) and, hence almost reaches the zero-line crossing point of the current.

In Fig. 22 the experimental and numerical results for current and voltage signals are plotted in the case of 0.4 mbar argon at 10 kV charging voltage. Again the measured current in the final part of the compression phase is about 20% lower than the computed value. The computations predict a minimum final radius of 26 mm at 20 μs while from magnetic field measurements (chapt. 4) we find t_{pinch} = 20 mm at 25 μs. In Fig. 22 we also show a plot of an "electrical" radius r_{el} defined by

$$\frac{\mu_0}{2\pi} \ell \ln \frac{R_0}{r_{el}} = \int_0^t v_p \, dt/i_p \qquad (38)$$

neglecting ohmic losses and assuming a thin sheet current distribution. The initial electrical radius r_{el} is calculated to 85 mm, while the quartz tube radius is 118 mm. This indicates that the current is not contained in a thin shell but has a finite distribution width. This is confirmed by the current distribution experimentally measured at 10 μs in argon at 0.4 mbar (Fig. 16). The electrical radius is approaching zero, because in eq. (38) we have neglected the ohmic plasma resistance which becomes non-negligible during the pinch phase due to the decreasing conducting cross section.

Figure 22 also shows the computed results with an initial ohmic resistance of 4 mΩ which reaches 20 mΩ in the pinch phase. The agreement between experimental and computed curves is now better but we also need to take into account the effect of ohmic resistance decreasing with rising plasma temperature.

6. Conclusion

In this note we have shown that the pinch dynamics in a plasma lens can be described and predicted with suitable z-pinch models. When designing plasma lenses for specific applications or when operating such a device on particle beams the knowledge and the control of the pinch dynamics are prerequisites. A well functioning computational model will therefore be of great value.

The SPE model satisfactorily simulates the dynamic pinch in the configuration of PL prototype II. Discrepancies like the observed deviations in current amplitudes are mainly due to neglecting the radial spread of current density during the implosion phase and the finite plasma resistivity as a function of plasma temperature. We intend in future to include these effects in the SPE model. More experimental results have to be compared with computations especially values of pinch radius obtained via magnetic field distribution measurements or via optical streak camera studies.

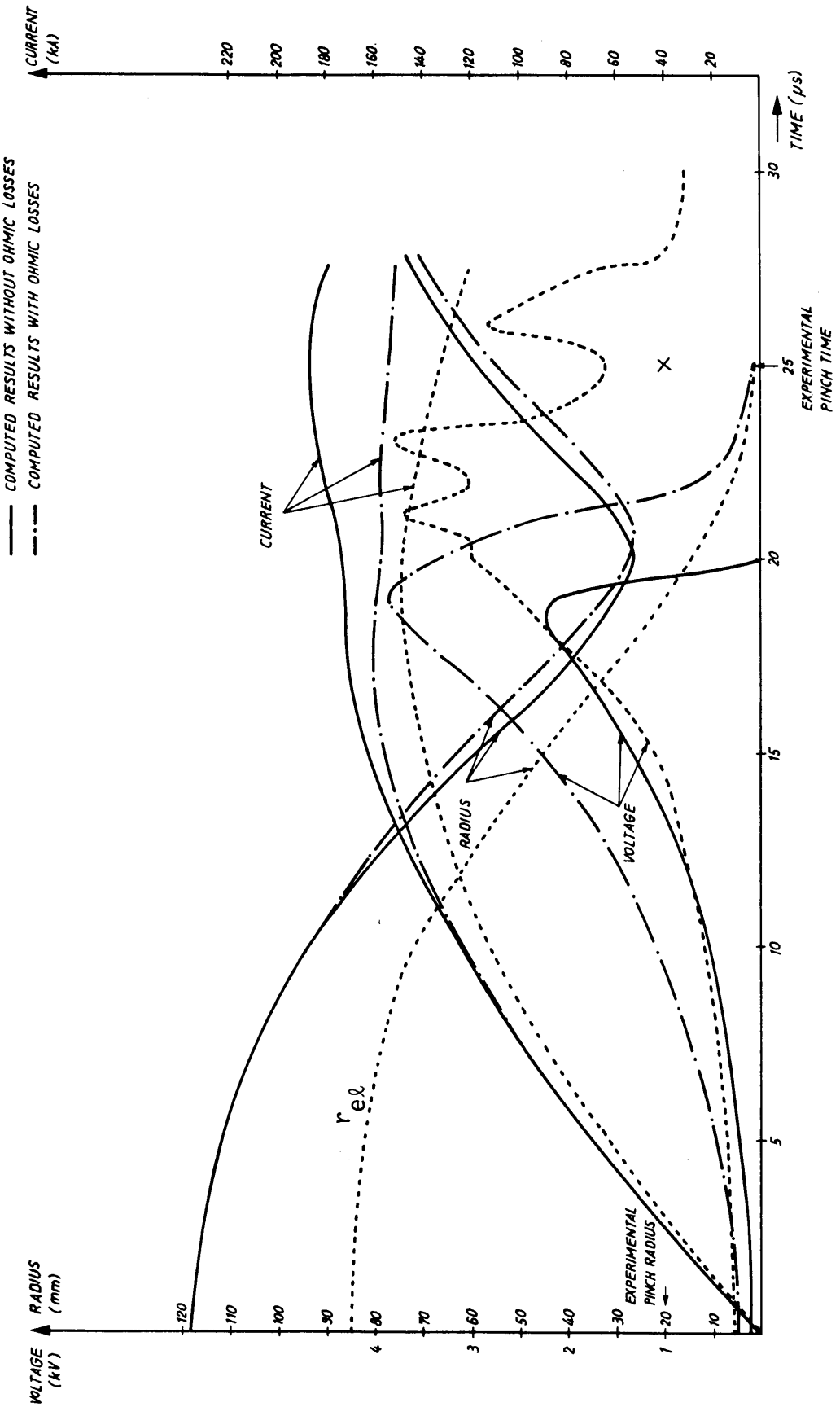

Figure 22 - Comparison of experimental and computed results for real time current, voltage and radius waveforms (Ar 0.4 mbar, V_o = 10 kV). The electrical radius $r_{e\ell}$ is calculated from eq. (38). Under the same conditions a pinch radius has been determined from the measured magnetic field distribution (x).

We have also realized that the SPE model in its present form is not well predicting the behaviour of PL prototype I (R_0 = 40 mm). Here the "slug"[8] model seems to be a better candidate. Reasons are mainly the much higher plasma temperature, produced in the much smaller pinch columns, the correlated higher ohmic resistance, and the higher pressure values used in these experiments compared with the studies on PL prototype II. Extrapolations beyond one size of order in lens cross-section seem to be difficult with a single z-pinch model.

Acknowledgements

We are very much indebted to Miss Hadorn and Mrs G. Knott for preparing the drawings of this note. We thank P. Billault and M. van Gulik for their help in preparing the magnetic field distribution measurements.

References

1. F. Krienen, Plasma lens for the Antiproton Source, Fermilab-$\bar{p}$-Note 137, 1981.

2. F. Christiansen, K. Frank, H. Riege, R. Seeböck, Studies of a plasma lens with pseudo-spark geometry for application in high energy accelerators, CERN/PS/84-10 (AA), 1984.

3. L. De Menna, G. Miano, B. Autin, E. Boggasch, K. Frank, H. Riege, Plasma lens for the CERN Antiproton Source, CERN/PS/84-13 (AA), 1984.

4. T. Miyamoto, Nucl. Fusion, 3 (1984) 337.

5. L.D. Landau, E.M. Lifshitz, Electrodynamics of continuous media, Pergamon Press, Oxford, 1960.

6. M. Rosenbluth et al., Los Alamos Scientific Rep. LA-1850, 1954.

7. J.C. Bowers, S.R. Sedore, ...SCEPTRE, Prentice-Hall, Inc., New Jersey, 1971.

8. D. Potter, Nucl. Fusion 18, 6 (1978), p. 813.